

# Novel Gradient Coils Designed Using a Boundary Element Method

MICHAEL POOLE, RICHARD BOWTELL

*Sir Peter Mansfield Magnetic Resonance Centre, Department of Physics and Astronomy,  
University of Nottingham, Nottingham NG7 2RD, United Kingdom*

**ABSTRACT:** Boundary element methods offer a powerful approach for designing gradient coils, allowing the generation of coils wound on arbitrarily shaped surface so as to produce any form of field variation that is consistent with Maxwell's equations. These methods are based on meshing the current carrying surface into an array of boundary elements. In this work, we have extended boundary element methods that have previously been used for coil design and integrated a powerful mesh generating program so as to produce coils with totally arbitrary geometry. Four examples are used to illustrate how the modified method provides a single versatile coil design protocol. These relate to the design of: i) shielded head gradients with highly asymmetric surface geometry that give the highest possible gradient field strengths; ii) very short, shielded gradient coils to allow improved access to the subject; iii) bi-planar coils generating highly asymmetric, stepped magnetic fields for use in fast imaging by multiple acquisition with micro- $B_0$  arrays (MAMBA); iv) an insertable set of head gradient coils with shoulder cut-outs. © 2007 Wiley Periodicals, Inc. *Concepts Magn Reson Part B (Magn Reson Engineering)* 31B: 162–175, 2007

**KEY WORDS:** gradient coils; boundary element method; BEM; stream function method; MAMBA

## INTRODUCTION

Magnetic field generating coils for use in magnetic resonance are numerous and varied. The principal, intense, highly homogeneous magnetic field is usually generated using superconducting coils and is oriented along the  $z$ -direction in the standard geometry. Other coils therefore usually only need to be concerned with modifying the  $z$ -component of the magnetic field,  $B_z$ .

Three orthogonal, linear gradient fields ( $B_z \propto x$ ,  $B_z \propto y$ , and  $B_z \propto z$ ) are used to encode the NMR signal spatially in imaging experiments. These are the 1st order terms in the spherical harmonic expansion of solutions to Laplace's equation,  $\nabla^2 B_z = 0$  (the 0th order spherical harmonic is a uniform field) for magnetic fields in the absence of sources. Magnetic field gradients are most simply generated by passing currents through Helmholtz and Golay ( $I$ ) coils. These discrete wire arrangements are derived analytically to annul other unwanted spherical harmonics. A description of the spherical harmonic decomposition of magnetic fields and the design of discrete wire coils was given by Roméo and Hoult (2).

Fast imaging modalities, such as echo-planar imaging (EPI) (3), demand increased performance from the gradient coils. The current in the gradient coils must be switched rapidly and therefore coils must be made with a low inductance so as to limit

Received 17 October 2006; accepted 6 February 2007

Correspondence to: Richard Bowtell; E-mail: richard.bowtell@nottingham.ac.uk

*Concepts in Magnetic Resonance Part B (Magnetic Resonance Engineering)*, Vol. 31B(3) 162–175 (2007)

Published online in Wiley InterScience (www.interscience.wiley.com). DOI 10.1002/cmrb.20091

© 2007 Wiley Periodicals, Inc.

the rise-time for a given applied voltage. In addition, coils must produce strong gradients so as to achieve high resolution. The strength of the field gradient produced may be increased simply by adding more turns of wire to the discrete coils mentioned above, but there is an associated increase in inductance; while the efficiency of a coil increases in proportion to the number of turns, the inductance scales approximately quadratically. This is the inherent conflict in gradient coil design: in order to maximize the efficiency of the coil, as well as keeping the inductance low, the extra wires must be spaced out, which decreases the accuracy with which the field gradient is produced. A goal of coil design is therefore to resolve this conflict and produce highly efficient coils, which generate a uniform field gradient over a large volume whilst having low inductance.

A “target field” approach was developed by Turner (4) following Turner and Bowley’s derivation of an appropriate mathematical formalism to describe the magnetic flux density,  $B_z$ , due to a current distribution on the surface of a cylinder using a Fourier-Bessel series (5). The current density has a unique solution which can be found from the Fourier transformed target field. Further work by Turner (6) on the target field approach allowed the inductance of a current distribution to be calculated in a similar way. This allowed coils of minimum inductance to be designed by specifying the desired field at an ensemble of points. The discrete nature of the target field causes the system to be ill-posed; quite different current densities may generate almost identical magnetic fields. Smoothing or apodisation functions are therefore used to remove high spatial frequency components in the Fourier transform of the current distribution, thereby reducing any oscillatory behaviour of the current density. Carlson et al. (7) parameterized the current density on the surface of a cylinder in terms of a small number of weighted, truncated sinusoidal harmonics in order to design finite length coils whilst minimising the inductance. Myers and Roemer showed that cylindrical gradient coils with asymmetrically positioned regions of uniformity (ROU) have high efficiency and reasonable gradient field uniformity (8). There are many more examples of coil designs that deviate from cylindrical geometry; planar gradients for NMR microscopy (9) and “open” MRI systems (10), gradients with a hemispherical geometry for brain imaging (11, 12), gradients with parabolic return paths to accommodate the shoulders (13), conical section surfaces linking the primary to the shield for short gradients (14), gradients with multiple regions of interest (ROI) (15) and MAMBA

coils for simultaneous acquisition of images from different sample regions (16).

All the methods mentioned above are based upon an invertible analytic relationship between the magnetic field (and other properties such as the inductance) and the current density. Other methods exist that only rely upon the forward relationship for obtaining the field from the currents. These numerical methods generally use a search process to find the optimal current density based on an initial estimate. Methods based on iterative search techniques such as simulated annealing (17), Monte Carlo approaches (18) and the genetic algorithm (19) have been used.

Pissanetzky (20) introduced a coil design methodology that allows the design of coils wound on an arbitrary surface using an inverse boundary element method (IBEM). This was recently extended by Lemdiasov and Ludwig (21, 22). Removing the reliance on coil symmetry opens up the possibilities for gradient coil design. Any coil that generates a specific magnetic field can be designed with this method, as long as the conducting surface encloses the ROU sufficiently to provide the desired field accuracy.

## THEORY

### Original Method

Here we begin by reproducing a brief outline of the mathematical formalism described in the original work (20). Pissanetzky discretizes the coil surface into a mesh of triangles, referred to as the “elements” of the surface. The points that lie at the corners of these elements are called the “nodes”, and small currents circulate around the nodes through the adjoining elements (see Fig. 4 in (22)). For each node,  $n$ , a basis function,  $\mathbf{f}_n(\mathbf{r})$ , is defined that describes each circulating current. Summing these together with the basis function weights,  $I_n$ , yields a representation the current density on the surface:

$$\mathbf{J}(\mathbf{r}) \approx \sum_{n=1}^N I_n \mathbf{f}_n(\mathbf{r}) \quad [1]$$

The stream-function of the current density,  $\varphi(\mathbf{r})$ , is also defined by the weights and an appropriate set of scalar basis functions,  $\varphi_n(\mathbf{r})$ . The weight,  $I_n$ , is in effect the value of the stream-function at the  $n$ th node.

Each current density basis function,  $\mathbf{f}_n(\mathbf{r})$ , is constructed from a set of  $N_n$  vectors,  $\mathbf{v}_{ni}$ , (for  $i = 1$  to  $N_n$ ) describing a unit current flowing through each of

the  $N_n$  triangular elements,  $\Delta_{ni}$ , associated with the  $n$ th node.

Every property of the coil that is dependent upon the current density can be written in terms of  $I_n$  and  $\mathbf{f}_n(\mathbf{r})$ . In particular, parameterization of the  $z$ -component of the magnetic field at position  $\mathbf{r}_k$ ,  $B_z(\mathbf{r}_k)$ , inductance,  $L$ , and torque vector,  $\mathbf{M}$  was described in Eqs. [12]–[21] of (22).

### Additions to the Method

The following sections describe the modifications to the previous work that were used in this study.

**Minimization of Power Dissipation.** The power dissipation,  $P$ , due to a current density distribution,  $\mathbf{J}(\mathbf{r})$ ,

$$P = \frac{\rho}{t} \int_S |\mathbf{J}(\mathbf{r})|^2 dS \quad [2]$$

is additionally parameterized. Here  $t$  is the thickness of the conducting layer, and  $\rho$  is the resistivity of the conducting material. The power loss is similar to the inductance, in that it is dependant on the square of the current density. The parameterized form of Eq. [2] for the meshed current distribution is similar to that describing the inductance (Eq. [18] in (22)):

$$P \approx \sum_{n=1}^N \sum_{m=1}^N I_n I_m P_{mn}, \quad [3]$$

where

$$P_{mn} = \frac{\rho}{t} \sum_i \sum_j \begin{cases} (\mathbf{v}_{mi} \cdot \mathbf{v}_{nj}) A_{mi}, & \Delta_{mi} = \Delta_{nj} \\ 0 & \Delta_{mi} \neq \Delta_{nj} \end{cases} \quad [4]$$

and  $A_{mi}$  is the area of the  $i$ th mesh element belonging to the  $m$ th node.

**Gauss-Legendre Numerical Integration.** Evaluation of the various properties of the current distribution requires calculation of an integral over the surface of each element. When the integrand does not vary over the element, the integral can be exchanged for the area of the triangle (e.g. Eq. [4]). In the case of the integral required for calculating the inductance, the integrand depends on the inverse of the distance between current sources. An area approximation can also be used when the distance involved in the integrand is much greater than the size of the elements. However, when the distances are small this

approximation is no longer accurate, especially for integration over the surfaces of neighbouring elements. In this work, integration by Gauss-Legendre quadrature (23) was therefore used to calculate the mutual inductance of two mesh elements when the distance between elements is less than 5 times the characteristic size of the elements. At this distance the approximation Eq. [35] in (22) is just 1% different to the value calculated by numerical integration. Adjacent triangles may however show a 20% difference in these values.

**The Functional.** Equation [5] shows the functional  $\Phi$  which was minimized in designing the coils described in this paper. It is the same as the functional used in previous work (22) with the addition of the weighted power loss term,  $\beta P$ , and removal of the field offset term,  $B_z^{\text{off}}$ .

$$\Phi = \frac{1}{2} \sum_{k=1}^K W(\mathbf{r}_k) [B_z(\mathbf{r}_k) - B_z^t(\mathbf{r}_k)]^2 + \frac{\alpha}{2} L + \beta P - \lambda_x M_x - \lambda_y M_y - \lambda_z M_z \quad [5]$$

This functional minimizes the square of the difference between the target field  $B_z^t(\mathbf{r}_k)$  and actual field  $B_z(\mathbf{r}_k)$  for  $K$  target field points, the stored energy (which for a 1A current is equivalent to half the inductance) and the power loss, as well as imposing torque-balancing.  $W(\mathbf{r}_k)$  is a weighting function that can be assigned any value for any target field position  $\mathbf{r}_k$ . Assigning a high value of  $W(\mathbf{r}_k)$  for a particular point causes more emphasis to be placed on the accuracy of  $B_z$  at this point.  $\lambda_x$ ,  $\lambda_y$ , and  $\lambda_z$  are the Lagrange multipliers that facilitate the cancellation of the  $x$ ,  $y$  and  $z$  components of the torque vector  $M_x$ ,  $M_y$ , and  $M_z$ .  $\alpha$  and  $\beta$  are user-defined parameters that control the relative importance ascribed to minimizing the stored energy and power loss, respectively.

**3D Contouring Algorithm.** As in other coil design methods the discrete wire-paths for the coil design are obtained by contouring the stream-function of the current density (24). The same process is performed here, but it must be carried out over the mesh elements. To achieve this, a contouring algorithm was written to individually contour each triangle of the surface. Each triangular element in 3D space is mapped to a 2D right-angled triangle of unit size using a coordinate transform ( $\mathbf{A}: \mathbb{R}^{(x,y,z)} \rightarrow \mathbb{R}^{(u,v)}$ ), and the values of the stream function,  $\phi$ , at the three corner nodes were used as the third coordinate to create a triangular, planar surface in  $(u, v, \phi)$  space. Identification of the lines of intersection of this

planar surface with surfaces of constant  $\varphi$  corresponding to each contour level, yields contour lines in  $(u, v, \varphi)$  space. The portion of these lines that reside within the triangle are transformed back into 3D with the inverse of the coordinate transform,  $\mathbf{A}^{-1}$  to give the small sections of wire for each element. This is repeated for all triangular elements to build up the full wire pattern.

**Minimum Wire Spacing.** The minimum wire spacing is often an engineering constraint in gradient coil design and can be found using a method similar to the 3D contouring algorithm. The wire separation in the  $t$ th triangle is found using a similar method to finding the wire paths. Two very close contour levels of known separation are created that cross the centre of each  $(u, v, \varphi)$  triangle and the resulting wire paths are then transformed to  $(x, y, z)$  space. Finding the distance between these two lines is then a simple geometric task and the separation is scaled by the ratio between the close wire separation and the actual contour level separation to obtain the minimum wire spacing allowed in the coil design.

## METHODS

### Mesh Generation

To make the most of this method, 3DS MAX<sup>®</sup> (Autodesk<sup>®</sup>, San Rafael, CA), a 3D graphics application was used to generate and export surface meshes to a text file. This powerful program made it simple to design any conceivable mesh geometry quickly, with any target region. The mesh generating protocol automatically defines the node ordering for each element in a consistent sense about the normal to the element. The text file is then read in to MATLAB<sup>®</sup> (Mathworks<sup>®</sup>, Natick, MA) to generate the basis functions, and matrices before solving for the stream-function values at the nodes.

### Coil Properties

It is a simple task to obtain the normalized magnetic field, stored energy, power loss, and torque properties of the meshed current distribution by multiplying appropriate matrices by the solutions,  $I_n$ . These properties relate to a gradient coil designed to generate a field of  $1 \text{ T m}^{-1} \text{ A}^{-1}$ , so to convert these to values relevant to an actual coil design it is necessary to apply a rescaling based on the actual magnetic field generated by the arrangement of wires forming the coil. Using the wire-paths obtained with the 3D con-

touring algorithm, and after ensuring correct directions of current flow, a Biot-Savart Law calculation can be performed to give the field at the target points,  $B_z^{BS}(\mathbf{r}_k)$ . This gives the field per unit current for the wire paths which can then be used to calculate the approximate real values for the efficiency,  $\eta$ , and thereby other properties of the coil.

A figure-of-merit (FOM) that characterizes the coil performance independent of the number of turns of wire used to build the coil, can be formed from the square of the efficiency of the coil divided by its inductance,  $\eta^2/L$ .

The accuracy of the field that the coil generates is measured by the maximum error in the field over the target region,  $\Delta B_z^{\max}$ . This error is expressed as a percentage of the maximum target field value,  $B_z^t(\mathbf{r}_k)$ , in the ROU:

$$\Delta B_z^{\max} = \max \left( \frac{|B_z^{BS}(\mathbf{r}_k) - B_z^t(\mathbf{r}_k)|}{\max(|B_z^t(\mathbf{r}_k)|)} \right) \times 100 \quad [6]$$

For comparison with other gradient coils the nonlinearity and nonuniformity of the gradient were also calculated using Eqs. [24]–[27] in (25).

To check the electrical properties of the wires, text files compatible with the program FastHenry (26) were generated. FastHenry is a multipole-accelerated impedance extraction program that takes the wires and their thicknesses and models the inductance and resistance of the coil. It is capable of modeling the skin depth effects at any driving frequency, but here only DC currents were employed.

Here we present coil designs based on four very different coil geometries so as to illustrate the versatility of the method.

### Example 1: Ultra-Efficient, Highly Asymmetric, Shielded Gradient Coils for Head Imaging

The first coil geometry was chosen to generate the highest possible gradient strengths for human head imaging by placing the current carrying surface as close to the region of interest (ROI) as possible. There are several head imaging modalities that would benefit from such increased efficiency, such as magnetic resonance angiography (27) or diffusion weighted imaging (28, 29). This example illustrates the ability of the new method to produce coils with highly asymmetric geometry. Figure 1(a) shows the geometry of the coil design. Current flow is parameterized via meshing of the primary and secondary surfaces. These surfaces are not connected, so as to

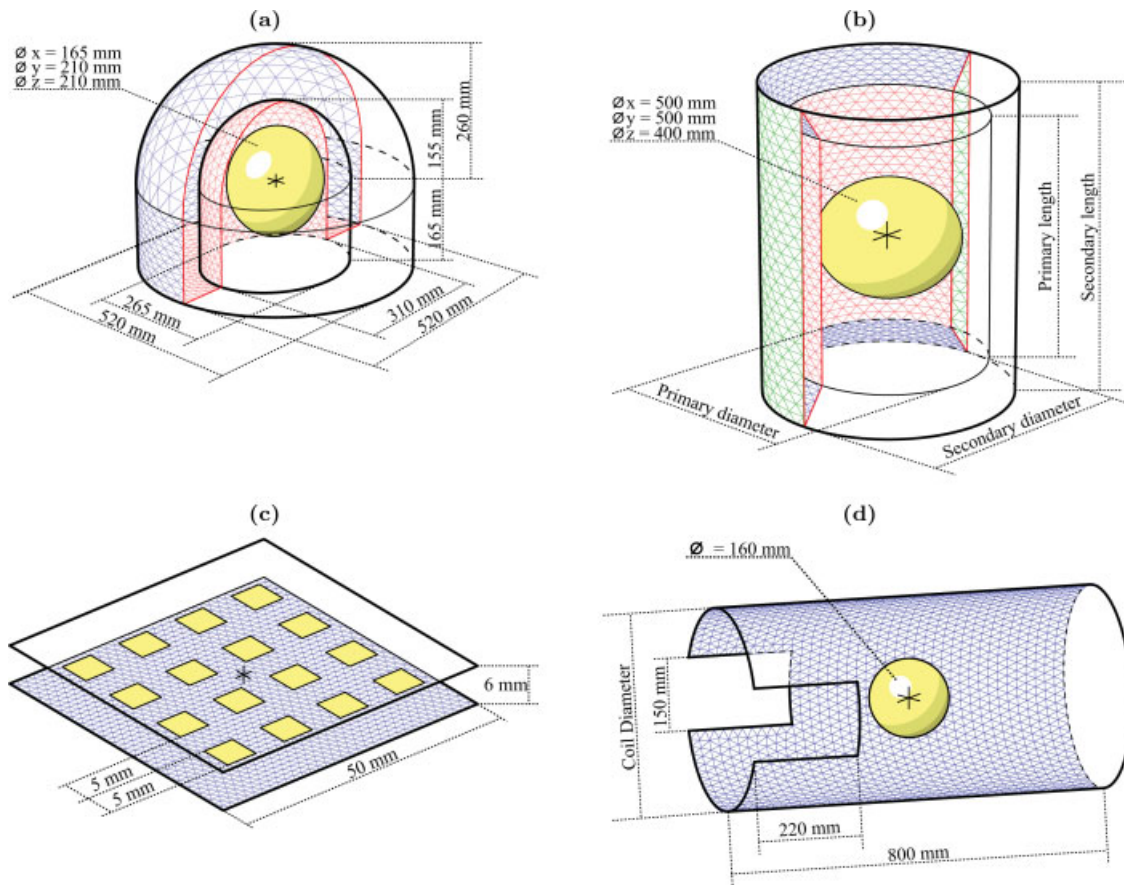


**Figure 1** Geometry of the (a) ultra-efficient shielded gradient coils, (b) ultra-short shielded gradient coils, (c) MAMBA coil and, (d) shoulder-slotted gradient coils. The triangles show half the discretized current carrying surfaces. The central spheroids and squares represent the target ROU. [Color figure can be viewed in the online issue, which is available at [www.interscience.wiley.com](http://www.interscience.wiley.com).]

ensure that no wires in the final coil designs cross from the primary to secondary surface as this would make coil construction unfeasible. The primary surface [red triangles in Fig. 1(a)] is created from a 310 mm diameter hemisphere and cylinder of length 165 mm squashed in the  $x$ -direction to be 265 mm wide. The elliptical cross-section was intended to reflect a head shape while providing a 50 mm gap between the head and the coil surface. The primary surface also has a flat annular surface attached to it, that fills the space between the inner and outer cylinders. A 520 mm diameter hemisphere, concentric with the inner hemisphere, with a 165 mm cylindrical extension forms the secondary surface. The coil surface has one defined edge on the primary and one on the secondary surfaces where they meet. The whole surface is discretized into 4,224 triangular elements and 2,162 nodes. The ROU is an oblate spheroid with a 165 mm width in the  $x$ -direction and 210 mm  $y$ - and  $z$ -widths, positioned concentrically with the

hemispheres of the surface, and contains 587 evenly distributed target points. The region of shielding (ROS) is formed from an ensemble of points evenly distributed over a 550 mm long cylindrical surface with a 640 mm diameter centred at 25 mm above the centre of the ROU in the  $z$ -direction.

### Example 2: Ultra-Short Gradients

The second test of the new method was to replicate the work of Shvartsman et al. (14) by generating a set of shielded, cylindrical gradient coils with very low length-to-diameter ratio. Their work involved producing coils consisting of four connected surfaces as shown in Figure 1(b); the inner surface is a short cylinder that generates the field gradient, the second surface is a longer cylinder that carries wires arranged so as to cancel stray fields from the the main coil and, the third and fourth surfaces are conical sections that

**Table 1** Theoretical Electromagnetic and Electrical Properties of the Ultra-Efficient X-, Y-, and Z-Gradient Coils<sup>a</sup>

Property	Gradient Coil		
	X	Y	Z
Stream-function contours, $N$	20	20	20
Efficiency, $\eta$ ( $\mu\text{T m}^{-1} \text{A}^{-1}$ )	327	287	456
Max. field error, $\Delta B_z^{\text{max}}$ (%)	5.0 (2.4)	5.0 (2.0)	5.0 (1.5)
Nonlinearity, nonuniformity (%)	5.0, 22.5	0.7, 21.0	25.6, 3.3
Inductance, $L$ ( $\mu\text{H}$ )	58 (63)	50 (56)	103 (112)
Min. wire spacing, $\Delta w_{\text{min}}$ (mm)	4.4	5.9	3.0
Resistance, $R$ ( $\text{m}\Omega$ )	76	74	83
x-Torque, $M_x$ ( $\text{N m A}^{-1} \text{T}^{-1}$ )	$-8.0 \times 10^{-6}$	$5.1 \times 10^{-3}$	$-3.5 \times 10^{-4}$
y-Torque, $M_y$ ( $\text{N m A}^{-1} \text{T}^{-1}$ )	$9.3 \times 10^{-4}$	$4.4 \times 10^{-5}$	$-6.5 \times 10^{-4}$
FOM, $\eta^2/L$ ( $\text{T}^2 \text{m}^{-2} \text{A}^{-2} \text{H}^{-1}$ )	$1.84 \times 10^{-3}$	$1.64 \times 10^{-3}$	$2.01 \times 10^{-3}$

<sup>a</sup> Bracketed values for  $\Delta B_z^{\text{max}}$  are the maximum field values at the shielding surface as a percentage of the maximum field in the ROU. Inductance values in brackets and resistances were calculated using FastHenry© (26) assuming that the coils were wound using 3 mm diameter copper wire.

connect the first and second surfaces at either end. In (14) the conical surfaces are used to remove the constant stream-function constraints at the ends of the primary and secondary coils. The dimensions of the coils and an analytical treatment of the design of coils of this geometry is provided in (14). In that work, the wires on the conical surface connecting the inner and outer cylindrical surfaces must be straight. Using the approach described here, wires may follow any path on the conical surface. The geometry employed by Shvartsman et al. (14) is duplicated here so as to illustrate the increase in coil performance resulting from the removal of the constraints on the current density imposed by the analytical approach. In applying the BEM approach, the surface was composed of 6080 triangular elements and 3040 nodes.

### Example 3: MAMBA Coils

The third example involved designing a coil for use with the MAMBA (multiple acquisition with Micro  $B_0$  Array) technique (30, 31). Implementation of MAMBA requires a coil which generates multiple regions of uniform magnetic field within the imaging volume. The magnetic field strengths are different within these regions, usually following a stepped profile across the imaging volume. Image data can thus be acquired simultaneously from the different regions. Lee et al. (30) developed a target field method for designing the coils needed for this novel imaging technique, and here we show that the BEM is capable of designing MAMBA coils with the same biplanar geometry as Lee et al. which have highly asymmetric field requirements [see Fig. 1(c)]. The 16 distinct tar-

get regions are each composed of a  $6 \times 6$  grid of target points, and the field in these regions is required to vary in 1mT steps from  $-7\text{mT}$  to  $+8\text{mT}$ . There are 5,200 triangular elements and 2,746 nodes in the surface.

### Example 4: Shoulder-Slotted Gradient Coils

The final design example is an insertable three-axis gradient coil set. This coil set is designed for head imaging on existing 3T and 7T systems and therefore must fit with pre-installed whole body gradient coils. The consequences for the coil design are that the 800 mm long cylindrical surfaces must have diameters lying between 390 mm and 450 mm, and therefore the shoulders of the subject must be accommodated by the design. Rectangular sections of 150 mm width and 220 mm length were therefore removed from the otherwise cylindrical shape. Figure 1(d) shows the geometry for the current carrying surface comprising between 5,456 and 5,678 elements with between 2,869 and 2,982 nodes. The region of uniformity used to define the field variation is a 160 mm diameter sphere containing 93 evenly distributed points. The X, Y, and Z coils are designed on cylindrical surfaces with diameters of 410.2, 416.2, and 422.2 mm respectively.

## RESULTS

### Example 1: Ultra-Efficient, Highly Asymmetric Gradient Coils for Head Imaging

Table 1 details properties of the ultra-efficient X-, Y-, and Z- head gradient coils and Figs. 2(a,c,e), show

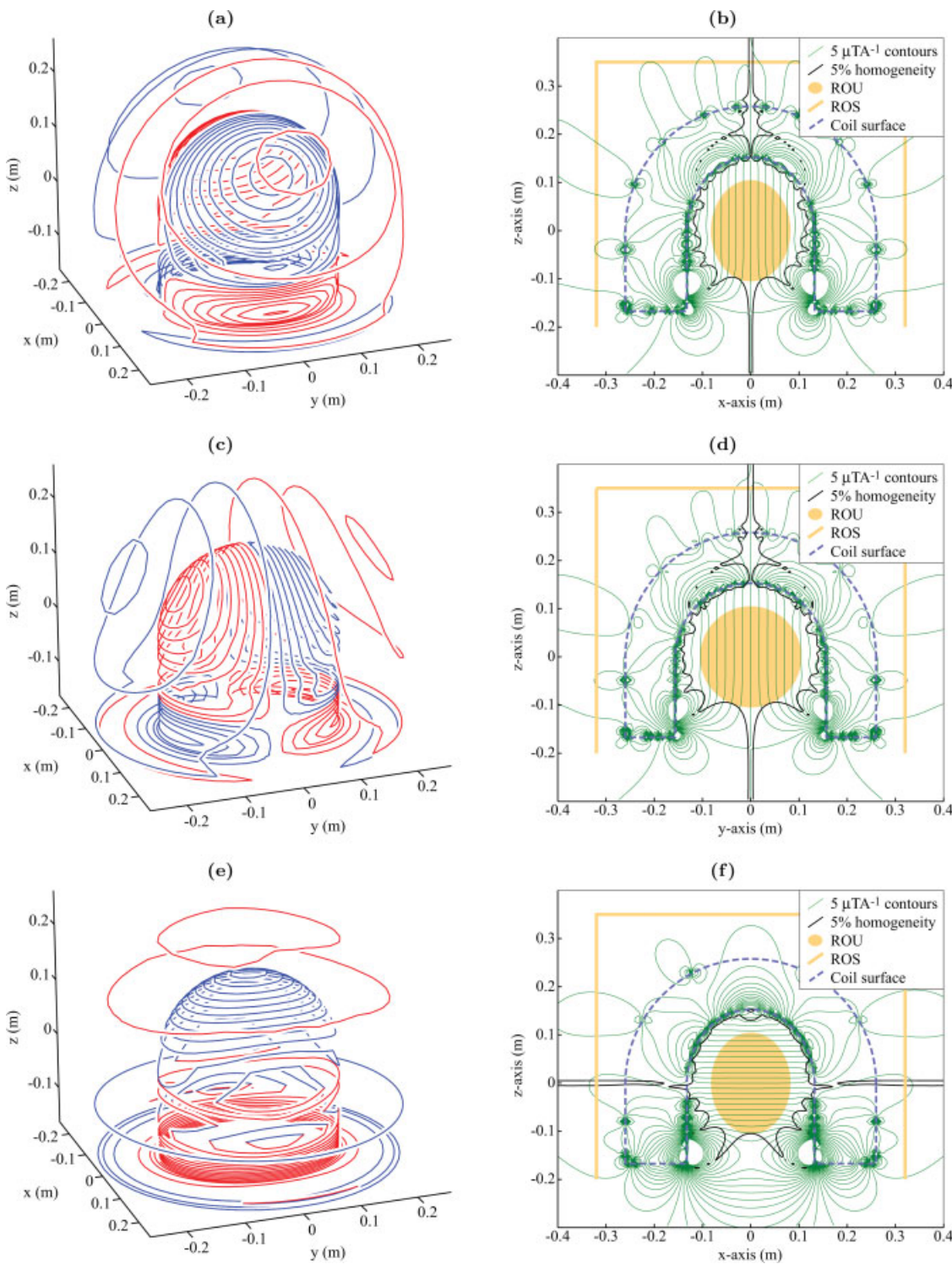


**Figure 2** Wire paths for the ultra-efficient (a) X-, (c) Y- and (e) Z-gradient coils. Red and blue colors are used to indicate wires in which there is a different sense of current flow. Also shown are contour maps of the magnetic field generated by unit current flow in the (b) X-, (d) Y- and (f) Z-gradient coils in the  $y = 0$ ,  $x = 0$ , and  $y = 0$  planes respectively. Contours are shown at  $5 \mu\text{T A}^{-1}$  steps. The solid black line shows the region inside which the field error is less than 5%. The ROU, ROS, and coil surface are also shown. [Color figure can be viewed in the online issue, which is available at [www.interscience.wiley.com](http://www.interscience.wiley.com).]

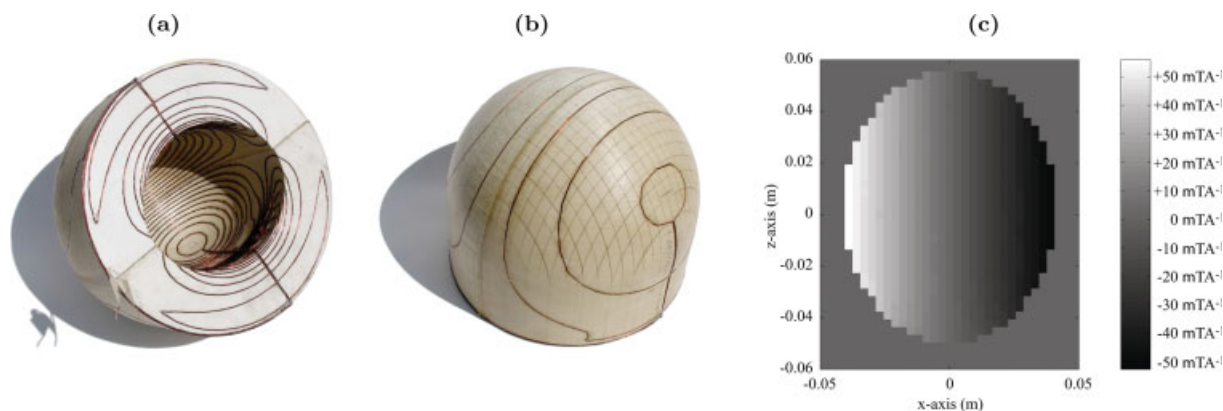


**Figure 3** (a) Inside and (b) outside views of the prototype ultra-efficient X gradient coil. (c) The field map in the  $y = 0$  plane is also shown with the scale on the right. [Color figure can be viewed in the online issue, which is available at [www.interscience.wiley.com](http://www.interscience.wiley.com).]

the wire paths for the X-, Y-, and Z- gradient coils respectively. The axial magnetic field distributions calculated in the  $y = 0$  plane ( $x = 0$  plane is used for the Y-gradient) by applying the Biot-Savart law to these wire paths, are shown in contour map form in Figs. 2(b,d,f), overlaid with a contour enclosing the region of less than 5% error in the field. A half-scale prototype of the X gradient coil, shown in Figs. 3(a,b), has been built and tested. The efficiency of the prototype coil was calculated by using a gradient echo based phase-mapping technique to measure the phase distribution within a water phantom for known drive currents. The phase is unwrapped and appropriately scaled to obtain maps of the magnetic field per unit current [see Fig. 3(c)]. The field map was used to calculate the efficiency of the prototype as  $1,379 \mu\text{T m}^{-1} \text{ A}^{-1}$  which implies an efficiency value of  $345 \mu\text{T m}^{-1} \text{ A}^{-1}$  when scaled to full size. The series inductance and resistance of the prototype were measured to be  $34 \mu\text{H}$ , and  $0.52 \Omega$  respectively with values of  $33 \mu\text{H}$ , and  $0.42 \Omega$  found when the prototype coil was modeled in FastHenry© with 0.9 mm diameter wire and at the same scale as the prototype.

### Example 2: Ultra-Short Gradients

Figures 4(a,c) show the wire patterns for ultra-short X and Z gradient coils (unfolded in the  $z$ -direction), while Figs. 4(b,d) are contour maps used to show the field produced by the ultra-short transverse and longitudinal gradient coils with the 5% error contour also shown. Table 2 lists the properties of the X, Y, and Z gradient coils.

### Example 3: MAMBA Coils

To compare with the coil in the original paper, a 2D MAMBA coil was designed to have an average field

error (using Eq. [16] in [16]) of less than 1.9%. Only power minimization was employed with 66 contours of the stream function chosen so as to give at least 1 mm spacing between the closest wires. With this coil, only 21 amps are needed to generate the same 1 mT step field. The wire paths for one of the two identical plates of the 2D MAMBA coil are shown in Fig. 5(a), and Fig. 5(b) shows the magnetic field that 21 A current flow in coils on both plates generate in the  $z = 0$  plane.

### Example 4: Shoulder-Slotted Gradient Coils

Efficiencies, inductances, resistances, FOM, and minimum wire spacings for the shoulder-slotted head gradient coils are given in Table 3 with the diameters of the coils and number of contour levels used in the design process. The wire paths of the X-, Y-, and Z-gradient coils are shown in Figs. 6(a,e), while Figs. 6(b,f) show plots of the field that they generate.

## DISCUSSION

The inner surface of the ultra-efficient coil set was placed 5 cm away from a  $16.5 \times 21.0 \times 21.0 \text{ cm}^3$  spheroidal region of uniformity spanning a typical head. The 5 cm gap is provided to accommodate an RF coil. The principle criterion is to position the wires as close to the head as possible. Practically, the arrangement chosen may be too claustrophobic. For this and for the sake of allowing visual interaction with the subject e.g. for fMRI, the geometry may also incorporate a window. The gradient fields produced by the ultra-efficient X, Y, and Z gradient coils are 2.0, 1.8, and 2.1 times stronger than previously

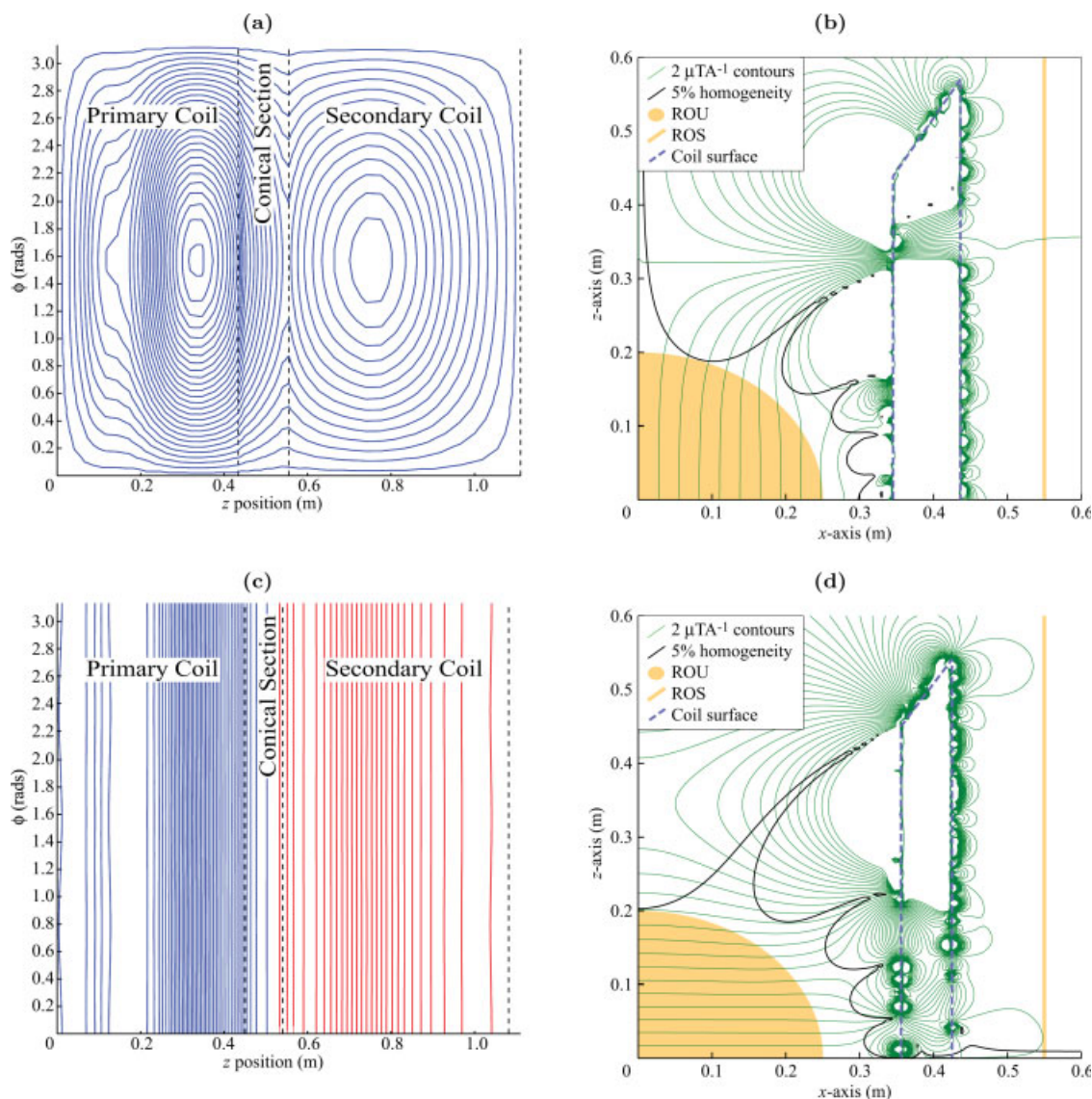


**Figure 4** Wire paths for the ultra-short (a) X- and (c) Z-gradient coils shown unfolded along the  $z$ -direction from  $z = 0$  on the inner surface to the conical surface and back to  $z = 0$  on the outer surface as in Fig. 6 (14). Contour maps in the  $y = 0$  plane of the magnetic field generated by unit current flow in the ultra-short (b) X and (d) Z gradient coils. Contours are shown using  $2 \mu\text{T A}^{-1}$  steps. The solid black line shows the region inside which the field error is less than 5%. The ROU, ROS, and coil surface are also shown. [Color figure can be viewed in the online issue, which is available at [www.interscience.wiley.com](http://www.interscience.wiley.com).]

described asymmetric head gradient coils (32) of equal inductance, but the new coils have much better homogeneity and are also shielded. The performance of these coils also compare favourably with dome gradient coils previously devised by Leggett et al. (12) where the ROU is significantly smaller and the coils are unshielded. The FOM for the new X-, Y-, and Z-gradient coils are 54%, 30%, and 60% higher respectively. The former on which the prototype ultra-efficient X gradient wires were laid was con-

structed with a rapid prototyping technique called Laminated (or Layered) Object Manufacturing (LOM<sup>TM</sup>) (Helisys, Torrance, CA) (33). For building highly asymmetric coil for real applications, a different fabrication method will need to be identified.

The increases in the FOM for the ultra-short X- and Z-gradient coils over those described in (14) are approximately 23% and 11% respectively. The improvement in the case of the X-gradient coil is primarily a consequence of the removal of restrictions

**Table 2** Theoretical Electromagnetic and Electrical Properties of the Ultra-Short X-, Y-, and Z-Gradient Coils<sup>a</sup>

Property	Gradient Coil		
	X	Y	Z
Stream-function contours, $N$	54	54	42
Efficiency, $\eta$ ( $\mu\text{T m}^{-1}\text{ A}^{-1}$ )	72.6	76.5	115.1
Max. field error, $\Delta B_z^{\text{max}}$ (%)	5.0 (3.6)	5.0 (3.5)	5.0 (2.7)
Nonlinearity, nonuniformity (%)	2.1, 22.5	2.6, 22.8	21.2, 0.2
Inductance, $L$ ( $\mu\text{H}$ )	713 (742)	798 (732)	1390 (1339)
Min. wire spacing, $\Delta w_{\text{min}}$ (mm)	5.6	5.6	5.5
Resistance, $R$ ( $\text{m}\Omega$ )	636	612	822
x-Torque, $M_x$ ( $\text{N m A}^{-1}\text{ T}^{-1}$ )	$-3.3 \times 10^{-5}$	$2.0 \times 10^{-6}$	$-1.34 \times 10^{-6}$
y-Torque, $M_y$ ( $\text{N m A}^{-1}\text{ T}^{-1}$ )	$-9.0 \times 10^{-3}$	$2.7 \times 10^{-4}$	$1.36 \times 10^{-6}$
FOM, $\eta^2/L$ ( $\text{T}^2\text{ m}^{-2}\text{ A}^{-2}\text{ H}^{-1}$ )	$7.40 \times 10^{-6}$	$7.33 \times 10^{-6}$	$9.52 \times 10^{-6}$

<sup>a</sup> Bracketed values for  $\Delta B_z^{\text{max}}$  are the maximum field values at the shielding surface as a percentage of the maximum field in the ROU. Inductance values in brackets and resistances were calculated using FastHenry© (26) assuming that the coils were wound using 3 mm diameter copper wire.

on the form of the current density on the conical linking surface which were imposed by the analytical approach employed in the previous work. Namely, the form of the stream-function meant that the connecting wires on the conical surface were straight. In the previous work (14), the Z gradient coil had no current loops on the conical surface. Here loops on the conical surface act to increase the FOM of the Z gradient coil. The shielding condition is different here than in the previous work, where it was based

upon calculating the residual eddy-current effect that allows some flux leakage onto conducting surfaces provided that the eddy-currents produce effects that can be corrected with gradient pre-emphasis.

Design of the 2D MAMBA coil is an inherently difficult problem; the form of the target field contains high spatial frequencies, and the highest spatial frequency present in the current density will always be higher than the maximum spatial frequency in the target field. This relationship is demonstrated for

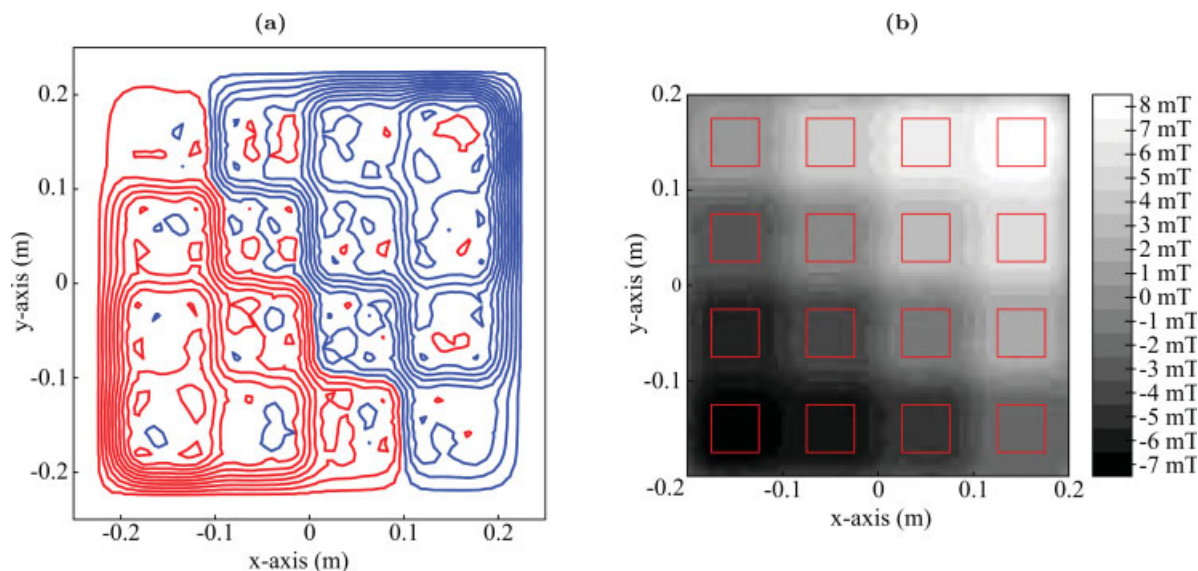


**Figure 5** (a) Wires of one plate of the 2D MAMBA coil (every 3rd wire is shown to aid in visualization). The full coil has 66 wires per plate. Red lines indicate wires with reversed current flow with respect to the blue lines. (b) A field map in the  $y = 0$  plane of the magnetic field generated by a current of 21.3 A flowing in the biplanar coil. The squares indicate the outline of the target regions. [Color figure can be viewed in the online issue, which is available at [www.interscience.wiley.com](http://www.interscience.wiley.com).]

**Table 3** Theoretical Electromagnetic and Electrical Properties of the Shoulder Slotted X-, Y-, and Z-Gradient Coils<sup>a</sup>

Property	Gradient Coil		
	X	Y	Z
Coil diameter (m)	0.410	0.416	0.422
Stream-function contours, $N$	14	14	14
Efficiency, $\eta$ ( $\mu\text{ T m}^{-1}\text{ A}^{-1}$ )	100	119	121
Max. field error, $\Delta B_z^{\text{max}}$ (%)	5.0	5.0	5.0
Nonlinearity, nonuniformity (%)	0.1, 16.6	4.9, 15.7	15.8, 3.2
Inductance, $L$ ( $\mu\text{H}$ )	60.3 (63.7)	62.3 (54.9)	51.8 (53.1)
Min. wire spacing, $\Delta w_{\text{min}}$ (mm)	3.7	5.9	7.8
Resistance, $R$ ( $\text{m}\Omega$ )	80.1	68.9	50.9
FOM, $\eta^2/L$ ( $\text{T}^2\text{ m}^{-2}\text{ A}^{-2}\text{ H}^{-1}$ )	$1.56 \times 10^{-4}$	$2.58 \times 10^{-4}$	$2.77 \times 10^{-4}$

<sup>a</sup> Inductance values in brackets and resistances were calculated using FastHenry© (26) assuming that the coils were wound using 3 mm diameter copper wire.

cylindrical geometries by Eq. [3] in (4). To represent the high spatial frequencies correctly in the current density, the coil surface must be discretized into small elements. This requirement is not met with the mesh used for the 2D MAMBA coils, so the wires have a jagged appearance. Despite this the coil wire-paths still generate an acceptably accurate field when the Biot-Savart Law is applied to them, and because the wires all lie on one surface the coil could be formed from a printed circuit board, which would greatly reduce any build tolerance errors over building by hand.

The system of equations used in to design gradient coils forms an ill-posed inverse problem in which the number of solutions is infinite. The ill-posed nature of the problem requires some form of regularisation to impose a preference on the solutions. With no regularisation of the system, the solutions tend to be oscillatory, highly sensitive to perturbations in the system variables, and consequently of little practical use. The type of regularisation employed here is in the form of minimisation of the inductance and/or resistance of the coil. This minimizes a scaled measure of the square of the solutions. There are other techniques that transform an ill-posed problem,  $\min_x \|Ax - b\|_2$ , into one that is well-posed. The most common of these is Tikhonov regularization (34, 35) which additionally minimizes the least-squares norm of the solutions;  $\min_x \{\|Ax - b\|^2 - \lambda^2 \|x\|^2\}$ . Minimization of the inductance in addition to the root-mean-squared field error is similar to a weighted Tikhonov regularization. Altering the regularization parameters  $\alpha$  and  $\beta$  in Eq. [5] changes the relative weighting placed upon minimization of the field error and the inductance and resistance. Figure 7 illustrates the tradeoff between the FOM of a coil and the maxi-

mum field error for varying  $\alpha$  that is produced for the X, Y, and Z ultra-efficient gradient coils. A similar relationship is evident when minimization of power dissipation is considered.

Requiring that the coil is torque-balanced reduces the size of the solution space. An additional parameter may be included in the functional [5] that permits the magnetic field to have a uniform field offset,  $B_z^{\text{off}}$  (see Eq. [1] in (22)). This is useful for designing asymmetric gradient coils that do not fully enclose the ROU, but is not used here as it creates some difficulties in implementing MRI sequences, including increased bandwidth for signal reception and larger field excursions during gradient switching leading to a lower threshold for peripheral nerve stimulation. If a field offset is permitted in the design of the ultra-efficient Z gradient coil, a coil can be designed with a 30.4  $\mu\text{T}$  offset at the centre of the ROU that has a FOM of  $2.96 \times 10^{-3}\text{ T}^2\text{ m}^{-2}\text{ A}^{-2}\text{ H}^{-1}$  (47% higher than with no field offset).

Since the surface is discretized into a number of small, flat triangular elements, the way in which this discretisation is performed is important (it is also possible to use curved surface elements (36)) The most important aspect of the discretisation is the number of elements (or nodes) used to approximate the surface and therefore the current density. More elements give a better approximation of the continuous current density, but this comes at the cost of increased computation time. The computation time increases approximately quadratically with the number of surface nodes,  $N$ , for the inductance and resistance matrices, and approximately linearly with  $N$  for the field matrix and the torque vectors. The time required to compute the field matrix also varies approximately linearly with the number of target

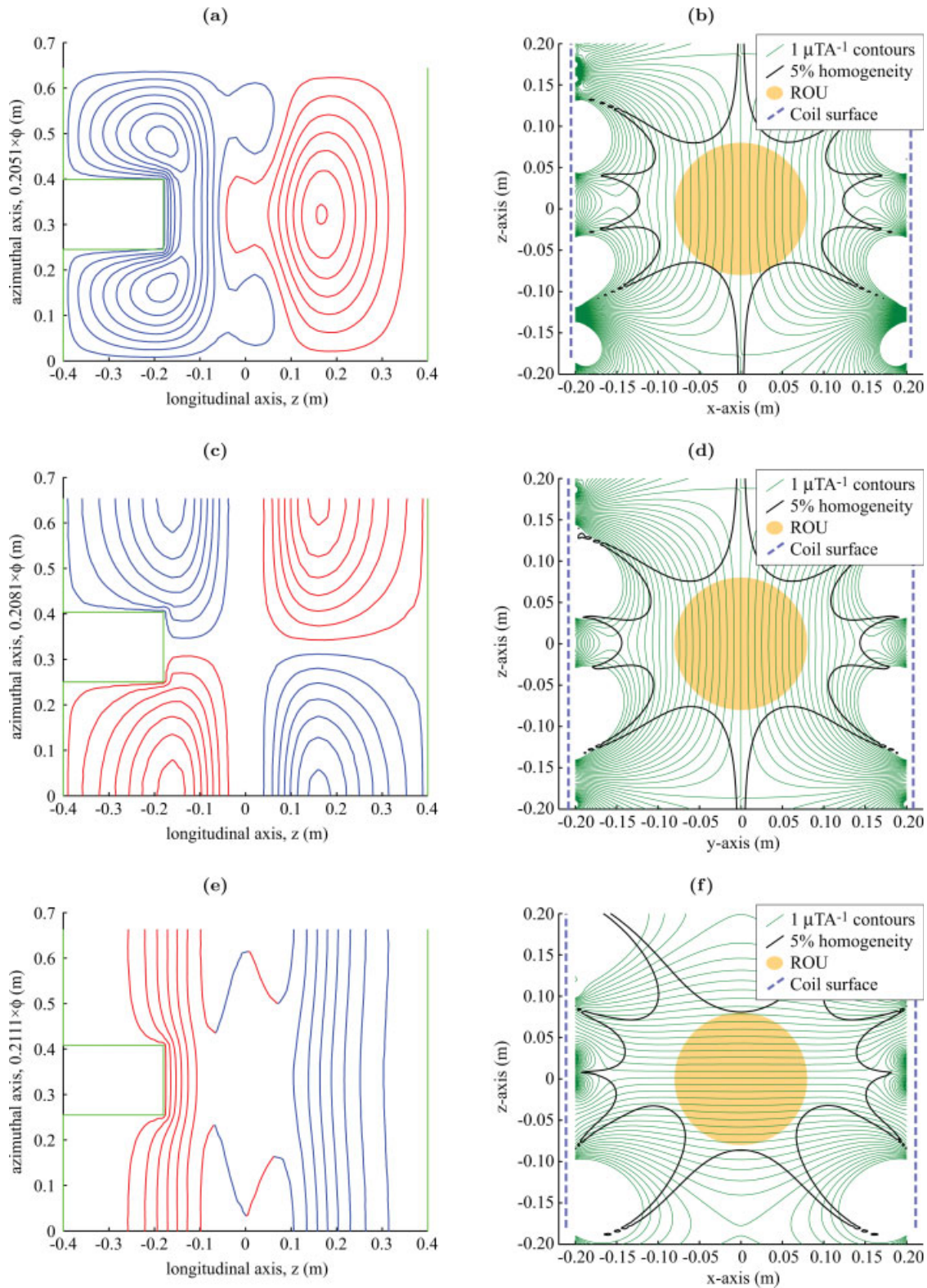


**Figure 6** Wire paths of one half ( $\phi > 0$ ) of the shoulder-slotted, head (a) X-, (c) Y- and (e) Z-gradient coils. Red wires have reversed current flow. Also shown are contour maps generated by unit current flow in the (b) X-, (d) Y- and, (f) Z-gradient coils in the  $y = 0$ ,  $x = 0$ , and  $y = 0$  planes respectively. Contours are shown at  $1 \mu\text{T A}^{-1}$  intervals. The solid black line shows the region inside which the field error is less than 5%. The ROU and coil surface are also shown. [Color figure can be viewed in the online issue, which is available at [www.interscience.wiley.com](http://www.interscience.wiley.com).]

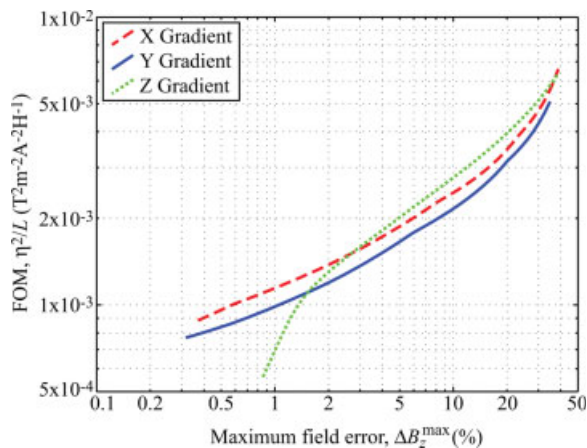


**Figure 7** Plot of the FOM and the maximum field error as  $\alpha$  is varied for the X, Y, and Z ultra-efficient gradients. [Color figure can be viewed in the online issue, which is available at [www.interscience.wiley.com](http://www.interscience.wiley.com).]

field points. In the four designs presented here, the number of nodes used was 2,162, 3,040, 2,746, and 3,033, and the number of target field points used was 1,085, 1,067, 576, and 93 for Examples 1, 2, 3, and 4 respectively. The computation of the matrices took approximately 16, 27, 37, and 16 h on a 2GHz Intel Pentium® 4 PC. This calculation only needs to be done once for each different geometry. Inverting the matrix to find the solution takes a few seconds.

In all these examples, the field error weighting function,  $W(\mathbf{r}_k)$ , in Eq. [5] is set to unity for all points. This means that no particular importance is placed on the accuracy of the field produced at different spatial locations. This function can be used to improve the performance of a particular coil design by decreasing the weighting for areas with inherently low field error. For example, the maximum field errors for the ultra-efficient coils will always occur at the open-end of the coil. By decreasing  $W(\mathbf{r}_k)$  in areas near the top of the ROU, these areas will exhibit larger, but still tolerable, field errors with a consequent increase in coil performance. Adjusting the weighting function for the ultra-efficient coils results in 4%, 7% and 23% increases in the FOM for the X, Y, and Z gradients respectively. Further slight improvements may be gleaned as the form of the weighting function used was empirically chosen. Similar adjustments of  $W(\mathbf{r}_k)$  for the X, Y, and Z ultra-short gradient coils results in 4%, 4%, and 9% increases in the FOM.

The BEM coil design method has also successfully been used to design cylindrical gradient and shim coils, spherical gradient and shim coils, shim coils with the same geometry as the shoulder slotted

coils in this paper, biplanar gradients, 1D MAMBA coils (16), shielded gradients with a central gap, hemispherical coils with a cylindrical extension (12) and biradial head-only gradients (37) which, in the interest of brevity, are not presented in this work.

## CONCLUSION

Using an inverse boundary element method (BEM) provides a way to design gradient, shim and other coils that generate specific magnetic fields free from all symmetry constraints. This is demonstrated here with the design of ultra-efficient and ultra-short gradient coils, 2D MAMBA coils, and shoulder-slotted head gradient and shim coils. The ultra-efficient coils generate a magnetic field gradient between 1.9 and 3.0 times stronger than previous head gradient coils at the same inductance (32). BEM improved the figure of merit of the ultra-short gradient coils by 12% to 24% over an analytic approach for the same geometry (14). The current needed to generate the same 2D MAMBA step field is 31% of the current used in (16) with the same wire separation. Finally, using the BEM to design shoulder-slotted head gradient and shim coils offers significant improvement over coils of purely cylindrical geometry. This versatility comes at the cost of increased computation time, and for symmetric designs it is simpler and quicker to use a more analytic approach. For this technique an efficient work-flow was created to allow the straightforward design of a coil of any geometry that generates any magnetic field.

## ACKNOWLEDGMENTS

We thank the EPSRC and Magnex Scientific Ltd. (now part of Varian, Inc.) for funding a studentship for M.P. We also thank Simon Harrison and Andrew Stone for assistance with construction of the rapid-prototyped gradient coil.

## REFERENCES

1. Golay MJE, Rumson NJ. 1971. Nuclear Magnetic Resonance Apparatus. US Patent 3,569,823.
2. Roméo F, Hoult DI. 1984. Magnet field profiling: analysis and correcting coil design. *Magn Reson Med* 1:44–65.
3. Mansfield P. 1977. Multi-planar image formation using NMR spin echoes. *J Phys C* 10:L55–L58.
4. Turner R. 1986. A target field approach to optimal coil design. *J Phys D: Appl Phys* 19:L147–L151.

5. Turner R, Bowley RM. 1986. Passive screening of switched magnetic field gradients. *J Phys E: Sci Instrum* 19:876–879.
6. Turner R. 1988. Minimum inductance coils. *J Phys E: Sci Instrum* 21:948–952.
7. Carlson JW, Derby KA, Hawryszko KC, Weideman M. 1992. Design and evaluation of shielded gradient coils. *Magn Reson Med* 26:191–206.
8. Myers CC, Roemer PB. 1991. Highly linear asymmetric transverse gradient coil design for head imaging. *Proc 10th Annual Meeting ISMRM*, p 711.
9. Bowtell R, Mansfield P. 1989. Minimum power, flat gradient pairs for NMR microscopy. *Proc 8th Annual Meeting ISMRM*, p 977.
10. Yoda K. 1990. Analytical design method of self-shielded planar coils. *J Appl Phys* 67:4349–4353.
11. Green D, Leggett J, Bowtell R. 2005. Hemispherical gradient coils for magnetic resonance imaging. *Magn Reson Med* 54:656–668.
12. Leggett J, Green D, Bowtell R. 2006. Insert dome gradient coils for brain imaging. *Proc ISMRM* 14: 779.
13. Morich M, Petropoulos L, Lampman D. 1996. Magnetic Resonance Insert Gradient Coils with Parabolic Returns for Improved Access. US Patent 5,485,087.
14. Shvartsman SH, Morich M, DeMeester G, Zhai Z. 2005. Ultrashort shielded gradient coil design with 3D geometry. *Concept Magn Reson B* 26:1–15.
15. Parker DL, Hadley JR. 2006. Gradient arrays for high performance multiple region MRI. *Proc ISMRM* 14: 521.
16. Lee KJ, Paley MNJ, Barber DC, Wilkinson ID, Griffiths PD. 2003. Target field design for MAMBA step fields. *Concept Magn Reson B* 20:1–8.
17. Crozier S, Doddrell M. 1993. Gradient coil design by simulated annealing. *J Magn Reson A* 103:354–357.
18. Konzbul P, Sveda K. 1995. Shim coils for NMR and MRI solenoid magnets. *Meas Sci Technol* 6:1116–1123.
19. Chladek J, Konzbul P, Osmera P, Gottvald A. 2000. Evolutionary and genetic optimization of NMR gradient and shim coils. *IEEE Trans Magn* 36:1102–1105.
20. Pissanetzky S. 1992. Minimum energy MRI gradient coils of general geometry. *Meas Sci Technol* 3:667–673.
21. Lemdiasov R, Ludwig R, Ferris C. 2005. A stream function method for gradient coil design. *Proc ISMRM* 13:854.
22. Lemdiasov R, Ludwig R. 2005. A stream function method for gradient coil design. *Concept Magn Reson B* 26:67–80.
23. Rathod HT, Nagaraja KV, Venkatesudu B, Ramesh NL. 2004. Gauss legendre quadrature over a triangle. *J Indian Inst Sci* 84:183–188.
24. Brideson MA, Forbes LK, Crozier S. 2002. Determining complicated winding patterns for shim coils using stream-functions and the target-field method. *Concept Magn Reson* 14:9–18.
25. Shvartsman SM, Brown RW, Cheng YC, Eagan TP, Fujita H, Morich MA, Petropoulos LS, Willig JD. 2001. Application of the SUSHI method to the design of gradient coils. *Magn Reson Med* 45:147–155.
26. Kamon M, Tsuk MJ, White JK. 1994. FastHenry: a multipole-accelerated 3-D inductance extraction program. *IEEE Trans MTT* 42:1750–1758.
27. Yucel EK, Anderson CM, Edelman RR, Grist TM, Baum RA, Manning WJ, Culebras A, Pearce W. 1999. Magnetic resonance angiography—update on applications for extracranial arteries. *Circulation* 100:2284.
28. Stejskal EO, Tanner JE. 1965. Spin diffusion measurements: spin echoes in the presence of a time-dependent field gradients. *J Chem Phys* 42:288–292.
29. Brugières P, Thomas P, Maraval A, Hasseini H, Combes C, Chafiq A, Ruel L, Breil S, Peschanski M, Gaston A. 2004. Water diffusion compartmentation at high  $b$  values in ischemic human brain. *AMJR* 25: 692–698.
30. Lee KJ, Paley MN, Wilkinson ID, Griffiths PD. 2002. Fast two-dimensional MR imaging by multiple acquisition with micro  $B_0$  array (MAMBA). *Magn Reson Imag* 20:119–125.
31. Paley MN, Lee KJ, Wild JM, Whitby EH, Griffiths PD. 2002. Interleaved pulsed MAMBA: a new parallel slice imaging method. *Magn Reson Med* 48:1043–1050.
32. Alsop DC, Connick TJ. 1996. Optimization of torque-balanced asymmetric head gradient coils. *Magn Reson Med* 35:875–886.
33. Feygin M. 1988. Apparatus and method for forming an integral object from laminations. US Patent 4,752,352.
34. Tikhonov AN. 1963. Solution of incorrectly formulated problem and the regularization method. *Soviet Math Dokl* 4:1035–1038.
35. Tikhonov AN. 1963. Regularization of incorrectly posed problems. *Soviet Math Dokl* 4:1624–1627.
36. Cobos SC, Marin L, Bowtell RW, Power H, Glover PM, Becker AA, Jones IA. 2006. Application of higher-order boundary element method to gradient coil design. *Proc BCISMRM* 12:P23.
37. Ungersma S, Xu H, Chronik B, Scott G, Macovski A, Conolly S. 2004. Shim design using a linear programming algorithm. *Magn Reson Med* 52:619–627.
38. Peeren GN. 2003. Stream function approach for determining optimal surface currents. *J Comp Phys* 191:305–321.